Journal of Applied Fluid Mechanics, Vol. 18, No. 4, pp. 1098-1114, 2025.
Available online at www.jafmonline.net, ISSN 1735-3572, EISSN 1735-3645.
https://doi.org/10.47176/jafm.18.4.2840

Numerical Study of a Supersonic Nozzle Gas Jet Laden with a Dry Powder Fire-extinguishing Agent Injected from a Bypass Injector

L. Zhang†, S. Wu, Y. Feng and H. Guan

School of Mechanical Engineering, Zhejiang Sci-Tech University, Hangzhou 310018, China

†*Corresponding Author Email: langzichsh@zstu.edu.cn*

ABSTRACT

To enhance the firefighting capabilities of traditional dry powder extinguishers, we incorporated an air-assisted supersonic nozzle, which is simulated using Euler-Lagrange interphase coupling to simulate the injection of firefighting agents into a supersonic, two-dimensional axisymmetric gas flow from a bypass injector. During the simulation, we employed our newly developed modified drag coefficient model, capable of accommodating a broad spectrum of particle Reynolds and Mach number conditions. Parameter studies show that an increase in the injector position, angle, and total pressure ratio generally causes a decrease in the average particle velocity $v_{p,a}$, and an increase in the dispersion Ψ_p and velocity unevenness Φ_{vp}; an increase in the total pressure ratio of the main nozzle leads to an increase in Φ_{vp} and $v_{p,a}$. However, under specific conditions, the monotonic dependency upon these parameters may be disrupted. For example, the performance indicators at the position of the injector near the nozzle throat and a larger total injector pressure ratio, as well as $v_{p,a}$ at smaller injection angles and Ψ_p at larger injection angles, may run counter to the monotonicity.

Article History

Received May 8, 2024
Revised September 11, 2024
Accepted October 20, 2024
Available online February 4, 2025

Keywords:

Corrected drag model
Dry powder fire extinguishing
Euler–Lagrange
Gas jet
Supersonic nozzle

1. INTRODUCTION

As society has rapidly developed, the number of high-rise buildings and chemical warehouses in cities has increased significantly. The increase in fire loss and expansion of the range of fire damage shows a clear pattern. Thus, professional, convenient, and efficient design of fire extinguishing equipment is of practical importance for promptly controlling fire situations, minimizing casualties, and effectively reducing losses (Haiqiang et al., 2014).

The main nozzle inlet of a traditional dry powder fire extinguisher is used to inject the fire extinguishing agent powder. However, such a configuration severely limits the spout speed and firing range of the particles. To address this issue, we propose a new technology called supersonic jet fire extinguishment applying bypass injection of dry powder, which involves the use of a de Laval nozzle to generate supersonic airflow while injecting fire extinguishing particles from the bypass injector located downstream of the nozzle throat. Because the localized low pressure in the main nozzle at this location has a natural priming effect on the particles and avoids the interference of the particles passing through the nozzle throat on the gas expansion across the speed of sound, the speed and range of the particles can be increased compared with those of traditional dry powder fire extinguisher nozzles.

For transient airflow with particle diameters in the range of tens of micrometres, added-mass force, Saffman force, and pressure gradient force play major roles in the motion of particles (Ling et al., 2011a, b, 2012; Bhattacharya et al., 2013). The inclusion of the Saffman force necessitates consideration of the resulting increase in the aerodynamic focusing of particles. The gas rarefaction effect it is essential to account for in the model of quasisteady force, given the broad range of flow parameters surrounding the particles, usually spanning continuous, transition, and free-molecular regimes. Concerning the unsteady force the difference in acceleration between particle and fluid phases necessarily generates to an unsteady (i.e., added mass) force acting on each fire extinguishing agent particle. Undoubtedly, the quasisteady (drag) force dominating particle motion should be incorporated primarily into the aerodynamic force model. Moreover, due to the significant changes in the particle Mach numbers and Reynolds number (Ma_p and Re_p) across the flow field, the gas rarefaction effect may have a significant impact on the quasisteady forces locally and, therefore, should be considered. However, in consideration of the complexity and relative insignificance of the viscous-unsteady force, it is

NOMENCLATURE

a	local speed of sound	T_g	temperature of gas
a_1	turbulence model constant	T_p	particle temperature
A_{inj}	injector inlet area	V_{cell}	volume of a grid cell
C_D	drag coefficient	V_p	volume of the nth computational particle
$C_{D,C}$	Clift's drag coefficient	w	uniform width
$C_{D,H}$	Henderson's drag coefficient	Z	particle mass loading at the injector inlet
$C_{D,P}$	Parmar's drag coefficient	Δ	parameter in the Boltzmann fitting function
$C_{D,std}$	standard drag coefficient	Δl_{min}	minimum grid size
C_M	added-mass force coefficient	β	turbulence model constant
C_p	specific heat of particle	B_1	turbulence model constant
d_p	particle diameter	γ	ratio of specific heats of gas
$e_{g,t}$	specific total energy of gas	μ	dynamic viscosity of gas
fr	correction factor of rarefaction effect	μ_t	turbulent eddy viscosity
F_1	blending function	ζ_p	radial coordinate of the computational particle
F_2	blending function	λ_{inj}	injector angle
G_{gp}	rate of work on the particle caused by the aerodynamic force	ν	turbulence model constant
G_s	nonboundary layer area mesh size	$v_{o,p}$	average particle velocity at the nozzle outlet
h_e	exit height	$v_{p,a}$	streamwise average velocity of particles
h_{in}	inlet height	$v_{p,inj}$	injected particle velocity
h_t	throat height	$v_{p,x}$	particle streamwise velocity component
k	turbulent kinetic energy	ρ_g	gas density
K	Saffman force constant	ρ_p	particle density
k_{eff}	effective thermal conductivity	σ_k	turbulence model constant
Kn_p	particle Knudsen number	σ_ω	turbulence model constant
l_c	convergent length	$\sigma_{\omega 2}$	turbulence model constant
l_d	divergent length	ς	normally distributed random number
l_{inj}	slot position	Φ_{vp}	particle velocity inhomogeneity
l_s	straight length	φ_p	particle volume fraction
Ma_p	gas Mach number	Ψ_p	dispersion of particles
N_{cs}	total number of computational particles in a certain region	ω	specific dissipation rate
N_p	real particle number represented by the computational particle	Ω	vorticity
NPR	nozzle pressure ratio	$\boldsymbol{F}_{am}$	added-mass force
ns	spread parameter	$\boldsymbol{F}_{pg}$	pressure-gradient force
Nu	Nusselt number	$\boldsymbol{F}_{qs}$	quasisteady force
p_i	static pressure at the injector inlet	$\boldsymbol{F}_{sa}$	Saffman force
p_{i0}	stagnation pressure at the injector inlet	$\boldsymbol{v}_g$	transient velocity of gas
p_p	static pressures at the primary nozzle inlet	$\boldsymbol{v}'_g$	fluctuation velocity of gas
p_{p0}	stagnation pressure at the primary nozzle inlet	$\bar{\boldsymbol{v}}_g$	time-averaged velocity of gas
P	pressure of gas	$\boldsymbol{x}_p$	position of the computational particle
Pr	Prandtl number	$\mathbf{I}$	identity matrix
Q_{gp}	rate of heat transfer to the particle from the gas	$\mathbf{S}$	deformation tensor
$q_{m,p}$	mass flow rate of particles	$\boldsymbol{\tau}_{eff}$	effective stress tensor
R_0	transition arc radius	$\boldsymbol{\tau}_m$	molecular stress tensor
r_e	exit radius	$\boldsymbol{\tau}_t$	turbulent stress tensor
r_{in}	inlet radius	2D	two-dimensional
r_t	throat radius	3D	three-dimensional
Re_p	particle Reynolds number	DPM	discrete phase model
R_g	gas constant	DRWM	discrete random walk model
s	molecular speed ratio	EL	Eulerian–Lagrangian
SPR	injection total pressure ratio	PSIC	particle-source-in-cell
t	time	SST	shear–stress transport
T	final time in the simulation		

reasonable to neglect its influence. In summary, when a model suitable for supersonic nozzle gas–solid flow is constructed, it is natural to first consider the dominant quasisteady (drag) force. Next, considering its relative

importance, the contribution of the Saffman force (especially for smaller particles) to the aerodynamic force should be considered. Because of the significant variation in flow parameters, the contributions of pressure-gradient force and added-mass force need to be considered. Lastly, the model should take the impact of turbulent vortices on particle motion into account. In view of the importance of quasisteady forces in particle motion, establishing an accurate and reasonable drag coefficient is crucial. Empirical formulas for the quasisteady drag coefficient were proposed by Henderson, Loth, and Parmar, with the first two models considering the aforementioned effects but having certain limitations on the ranges of the particle Reynolds and Mach numbers. The Parmar model only considers the compressibility and inertial effects of the gas, without considering rarefaction effects. Our recent work has led to the development of a modified drag model that considers the combined effects of gas compressibility, rarefaction, and inertia, based on existing drag coefficient models, and its validity is pending further investigation.

Extensive research has shown the efficiency of fire suppression is largely dependent on three key factors: the extinguishing agent properties, the design of the main nozzle or ejector, and the conditions of injection. In terms of geometric conditions, factors such as the position of the main nozzle outlet and the convergence angle of the mixing section significantly affect the performance of the injector. The optimal position of the main nozzle outlet is not only proportional to the throat diameter of the mixing section but also increases with increasing mainstream pressure. However, the performance of the injector is highly sensitive to the convergence angle of the mixing section, especially near the optimal operating point (Zhu et al., 2009). By adjusting the inlet diameter and convergence length, the detrimental influence of the powder carrier gas on particle acceleration is minimized. An increase in the intake pipe diameter and convergence length leads to more thorough gas–particle mixing and heat exchange, more uniform airflow at the throat, and greater particle temperature and velocity. As the ratio of expansion increases and the nozzle length diverges, the maximum particle collision speed increases accordingly, with a reciprocal relationship observed between particle impact velocity and particle size or density (Jebakumar & Abraham, 2016). The shape of the extinguishing agent affects the extinguishing efficiency. Particles that are closer to spherical and have smaller volumes can accelerate more fully in the gas (Cao et al., 2020). Conversely, the larger the particle volume is, the more apparent the lag representation of the particle in the jet flow (Wang et al., 2021). In terms of the nozzle operating parameters, the injected particle velocity has a negligible impact, whereas the particle mass flow rate significantly affects the particle-laden airflow (Parmar et al., 2011). Previous studies have focused mainly on the effects of particle properties, injection velocity and mass flow rate, main nozzle geometry, and operation in traditional dry powder injection methods. However, there is a lack of research on parameters such as the position of the injector, injection angle, main nozzle and injector pressure in the bypass-injected fire extinguishing agent supersonic injection method, and these parameters may have a significant effect on particle acceleration and dispersion. The geometric structure and operating parameters of the injector are important factors for the new fire extinguishing technology proposed in our study, and the analysis of these parameters has not been completed in our previous research.

This study aims to explore the characteristics of a two-dimensional axisymmetric supersonic nozzle carrying a fire extinguishing agent injected through a bypass. Using the Euler–Lagrange approach and the particle point approach (PPA) for the particle phase, a gas–solid two–way coupled model is established that incorporates the gas-phase SST k–ω turbulence model (Gilbert et al., 1955) and the particle source–in-cell method (Zhang et al., 2018). Our newly developed drag coefficient model, which accounts for gas inertia effect, rarefaction effect, and compressibility effect, is used to model the quasisteady force, and further model comparisons and validations are conducted (Parmar et al., 2010). To account for the impact of turbulent stochastic pulsations on the motion of the micron-sized particles, a particle random trajectory model is employed. This study defines three jet performance indicators closely associated with the fire extinguishing efficiency, including the average particle velocity, velocity inhomogeneity, and dispersion. On the basis of these indicators, this study quantitatively analyses the effect of the injector geometric structure and operational conditions for example the injector position, injection angle, main nozzle inlet pressure, and injector pressure, on these performance indicators. Additionally, this study provides a detailed analysis of the impact of these parameters and conducts a centre-of-mass calculation of the particle system to quantitatively analyse the relationship between the position of the particle phase centre of mass and its motion. Furthermore, the study forms specific parameter selection strategies for different flame types.

This paper proceeds as follows. Section 2 details the development of the jet flow framework, including the geometric model of the nozzle, the mathematical model, and the discrete phase physical model. Next, Section 3 outlines the numerical solution approach and validation, including a comparison of various drag coefficient models. The simulation results and corresponding analyses are presented in Section 4, which elucidate the impact of bypass injector design parameters (injection position l_{inj}, angle λ_{inj}) and injection conditions (main nozzle pressure ratio, *NPR*, and injector stagnation pressure ratio, *SPR*) in the flow field and jet performance indicators. Finally, the key findings are summarized in Section 5.

2. INTER-PHASE COUPLED MODELLING

2.1 Gas Phase Equations

In this study, the gas phase can be considered a continuous medium, and its flow is governed by the Navier–Stokes equations (Foias et al., 2002), incorporating the conservation relations for mass, momentum, and energy, namely:

$$\frac{\partial \rho_g}{\partial t} + \nabla \cdot \left(\rho_g \bar{\boldsymbol{v}}_g\right) = 0 \tag{1}$$

$$\frac{\partial}{\partial t}\left(\rho_g \bar{\boldsymbol{v}}_g\right)+\nabla\cdot\left(\rho_g \bar{\boldsymbol{v}}_g \bar{\boldsymbol{v}}_g\right)=-\nabla p+\nabla\cdot\boldsymbol{\tau}_{eff}-\frac{1}{V_{cell}}\sum N_p \boldsymbol{F}_{gp} \tag{2}$$

$$\frac{\partial}{\partial t}\left(\rho_g e_{g,t}\right)+\nabla\cdot\left[\left(\rho_g e_{g,t}+p\right)\bar{\boldsymbol{v}}_g\right]=\nabla\cdot\left(k_{eff}\nabla T_g+\boldsymbol{\tau}_{eff}\cdot\bar{\boldsymbol{v}}_g\right)-\frac{1}{V_{cell}}\sum N_p\left(Q_{gp}+G_{gp}\right) \tag{3}$$

where $\bar{\boldsymbol{v}}_g$ represents the time-mean velocity; ρ_g and p represent the gas density and pressure, respectively; V_{cell} denotes the cell volume; N_p denotes the number of computational actual particles; with $e_{g,t}$ being the total specific energy; k_{eff} represents the thermal conductivity including turbulence effects; $G_{gp}=\boldsymbol{F}_{gp}\cdot\bar{\boldsymbol{v}}_g$ is the power exerted on the computational particle due to the aerodynamic force; Q_{gp} represents the interphase heat transfer rate; and $\boldsymbol{\tau}_{eff}$ signifies the total stress tensor, including Reynolds stress tensor $\boldsymbol{\tau}_t$ and molecular contribution $\boldsymbol{\tau}_m$, where $\boldsymbol{\tau}_t$ and $\boldsymbol{\tau}_m$ are expressed as

$$\boldsymbol{\tau}_m=\mu\left[\nabla\bar{\boldsymbol{v}}_g+\left(\nabla\bar{\boldsymbol{v}}_g\right)^T-\frac{2}{3}\mathbf{I}\nabla\cdot\bar{\boldsymbol{v}}_g\right] \tag{4}$$

$$\boldsymbol{\tau}_t=\mu_t\left[\nabla\bar{\boldsymbol{v}}_g+\left(\nabla\bar{\boldsymbol{v}}_g\right)^T-\frac{2}{3}\mathbf{I}\nabla\cdot\bar{\boldsymbol{v}}_g\right]-\frac{2}{3}\rho_g k\mathbf{I} \tag{5}$$

where μ_t denotes the eddy viscosity, $\mathbf{I}$ denotes the unity matrix, k denotes the turbulent kinetic energy and ω denotes the rate of specific dissipation. In view of the reliability and acceptable accuracy of the SST k–ω turbulence model (Gilbert et al., 1955) in handling complex jet flows (Soliman et al., 2011), our study adopts this turbulence model. In this model, the expressions of k and ω are as follows:

$$\frac{\partial(\rho_g k)}{\partial t}+\nabla\cdot\left(\rho_g k\bar{\boldsymbol{v}}_g\right)=\boldsymbol{\tau}_t:\nabla\bar{\boldsymbol{v}}_g-\rho_g\beta_1 k\omega+\nabla\cdot\left[(\mu+\sigma_k\mu_t)\nabla k\right] \tag{6}$$

$$\frac{\partial(\rho_g\omega)}{\partial t}+\nabla\left(\rho_g\omega\bar{\boldsymbol{v}}_g\right)=\frac{\rho_g v}{\mu_t}\boldsymbol{\tau}_t:\nabla\bar{\boldsymbol{v}}_g-\rho_g\beta\omega^2+\nabla\cdot\left[(\mu+\sigma_\omega\mu_t)\nabla\omega\right]+2(1-F_1)\rho_g\sigma_{\omega2}\frac{1}{\omega}\nabla k\cdot\nabla\omega \tag{7}$$

The expression of μ_t is as follows:

$$\mu_t=\frac{\rho_g a_1 k}{\max(a_1\omega,\Omega F_2)} \tag{8}$$

Where Ω denotes vorticity, a_1, β_1, β, σ_k, σ_ω, and $\sigma_{\omega2}$ represent model parameters and where F_1 and F_2 represent blending coefficients. Work of Menter gives additional information on the SST *k–ω* turbulence model (Gilbert et al., 1955).

Finally, considering that the research subject of this paper is high-speed compressible flow, the gas density is calculated via the ideal gas state equation. Both the molecular viscosity and thermal conductivity of the gas are calculated via the three-coefficient Sutherland formula, which considers the temperature effect (Sutherland, 2009).

2.2 Particle Phase Equations

The discrete phase model is utilized to track the motion of particles Considering that sizes of particles being studied are around 10–100 μm , thus the velocity of particles can reach several hundred metres per second, particle rotational motion is assumed to be negligible.

2.2.1 Aerodynamic Force

Building on the previous work of Parmar (Parmar et al., 2010, 2011) and Ling (Ling et al., 2011a, b), the computational particles are subject to overall aerodynamic forces, which are simulated using a particle point force model as follows:

$$\boldsymbol{F}_{gp}=\boldsymbol{F}_{qs}+\boldsymbol{F}_{am}+\boldsymbol{F}_{pg}+\boldsymbol{F}_{sa} \tag{9}$$

where $\boldsymbol{F}_{am}$, $\boldsymbol{F}_{qs}$, $\boldsymbol{F}_{sa}$, and $\boldsymbol{F}_{pg}$ represent the added-mass force, quasisteady force, Saffman vector force, and pressure-gradient force. The $\boldsymbol{F}_{qs}$ is expressed as:

$$\boldsymbol{F}_{qs}=\frac{\pi}{8}\left(d_p\right)^2 C_D\rho_g\left(\boldsymbol{v}_g-\boldsymbol{v}_p\right)\left|\boldsymbol{v}_g-\boldsymbol{v}_p\right| \tag{10}$$

where C_D denotes the drag coefficient, d_p denotes the particle diameter, and $\boldsymbol{v}_g$ is the instantaneous gas velocity, which represents the summation of the fluctuating velocity $\boldsymbol{v'}_g$ and the mean velocity $\bar{\boldsymbol{v}}_g$. $\boldsymbol{v}_p$ denotes the particle velocity. Considering the turbulent diffusion influence on motion of particle, a random tracking method, namely, the discrete random walk model (DRWM) is adopted, which generates a fluctuation velocity $\boldsymbol{v'}_g$, thereby yielding a random trajectory for each particle. In Cartesian coordinate system, expression for the isotropic component of the pulsating velocity is $\boldsymbol{v'}_g=\varsigma\sqrt{2k/3}$, ς represent the normally random distributed number, and k denotes turbulent kinetic energy, at corresponding locations throughout the flow field (Gosman & Loannides, 1983).

$\boldsymbol{F}_{am}$ is computed as follows:

$$\boldsymbol{F}_{am}=C_M V_p\left(\frac{d\rho_g\boldsymbol{v}_g}{dt}-\frac{d\rho_g\boldsymbol{v}_p}{dt}\right) \tag{11}$$

where V_p is the computational particle volume and where C_M is the added-mass coefficient, with a value of 0.5 for spherical particles.

Expression for $\boldsymbol{F}_{pg}$ is

$$\boldsymbol{F}_{pg}=-V_p\nabla p \tag{12}$$

$\boldsymbol{F}_{sa}$ is given as

$$\boldsymbol{F}_{sa}=C_M V_p\frac{2K(\rho_g\mu)^{\frac{1}{2}}}{d_p(\mathbf{S}\cdot\mathbf{S})^{\frac{1}{4}}}\left(\mathbf{S}\cdot\left(\boldsymbol{v}_g-\boldsymbol{v}_p\right)\right) \tag{13}$$

where $K=2.595$, $\mathbf{S}$ denotes the deformation tensor (Sutherland, 2009).

2.2.2 Heat Transfer and Particle Motion

The particles motion is governed by Newton's second law, which can be mathematically formulated as:

$$m_p\frac{d\boldsymbol{v}_p}{dt}=\boldsymbol{F}_{qs}+\boldsymbol{F}_{am}+\boldsymbol{F}_{pg}+\boldsymbol{F}_{sa} \tag{14}$$

$$\boldsymbol{v}_p=\frac{d\boldsymbol{x}_p}{dt} \tag{15}$$

where m_p is the mass of the computational particle and where $\boldsymbol{x}_p$ is the position vector.

The expression for convective heat transfer from the gas to a particle is as follows:

$$Q_{gp}=\frac{\pi\mu c_{gp}d_p(T_g-T_p)Nu}{Pr} \tag{16}$$

Table 1 Detailed dimensional data of the two-dimensional axisymmetric nozzles

l_s, mm	l_c, mm	l_d, mm	r_{in}, mm	r_t, mm	r_e, mm	w_{inj}, mm
46	69	138	11.5	8.05	16.1	6.05

Table 2 Inlet pressure settings and particle inlet conditions

p_p, atm	p_{p0}, atm	p_i, atm	p_{i0}, atm	C_p, kg^{-1}·K^{-1}	ρ_p, kg^{-1}·K^{-1}	$v_{p,inj}$, m/s
46	69	138	11.5	1280	1803	100

where c_{gp} is the specific heat of the gas at constant pressure, T_g and T_p represent the gas and particle temperatures, respectively, and the Prandtl number is calculated as $Pr = 4\gamma/(9\gamma - 5)$. Given the concise expression and acceptable accuracy of Ranz and Marshall's correlation (Ranz & Marshall, 1952), we use Pr to calculate the Nusselt number Nu.

2.2.3 Drag Force Coefficient Model

This study utilizes a recently developed drag coefficient model that accounts for the concurrent influences of gas compressibility effect, rarefaction effect, and inertia effect. It integrates the characteristics of the Clift, Parmar, and Henderson models.

$$C_D = \begin{cases} f_r(Kn_p)C_{D,C}, & Re_p \le 1500 \\ f_r(Kn_p)C_{D,P}, & Re_p > 1500, M_p \le 1.75 \\ C_{D,H}, & M_p \ge 1.75 \end{cases} \tag{17}$$

where f_r is the correction factor that modifies the drag coefficient in the transitional and free molecular flow regimes and is expressed as follows:

$$f_r(Kn_p) = \begin{cases} 1, & \frac{M_p}{Re_p} < 0.1 \\ \frac{1}{1 + Kn_p[2.492 + 0.84exp(-1.74/Kn_p)]}, & \frac{M_p}{Re_p} \ge 0.1 \end{cases} \tag{18}$$

Re_p, M_p, and Kn_p are defined as follows:

$$Re_p = \frac{\rho_g |\boldsymbol{v}_g - \boldsymbol{v}_p| d_p}{\mu} \tag{19}$$

$$M_p = \frac{|\boldsymbol{v}_g - \boldsymbol{v}_p|}{a} \tag{20}$$

$$Kn_p = 1.256\sqrt{\gamma}\frac{M_p}{Re_p} \tag{21}$$

Where a denotes the speed of local sound, μ and γ represent dynamic viscosity and specific heat of the gas. Additionally, $C_{D,P}$, $C_{D,C}$, and $C_{D,H}$ denote the drag coefficient expressions of Parmar, Clift, and Henderson, respectively, within the aforementioned parameter ranges (Henderson, 1976; Clift et al., 1978; Parmar et al., 2010).

3. NUMERICAL APPROACH AND SIMULATION CONFIGURATION

3.1 Numerical Approach

ANSYS Fluent is used as the solver in this study, where gas phase is computed under an implicit density-based algorithm. The convective fluxes are discretized using the QUICK and third-order MUSCL schemes.

Furthermore, a nonsteady tracking method with gas-phase time steps is employed on the basis of the DRWM model, tracking each discrete phase particle in a Lagrangian framework and allowing for the inclusion of turbulent fluctuations in particle motion within this framework.

First, we perform the steady-state gas phase flow simulation. Following the initiation of particle injection, the simulation of two-phase flow is performed until solver meets convergent criterion.

We conduct a parametric study, particles are introduced from the bypass, change geometric parameters of the bypass injector (injection position l_{inj}, angle λ_{inj}) and the injection conditions (main nozzle pressure ratio *NPR*, injector total pressure ratio (*SPR.*)). Figures 1a-c present schematic diagrams of the nozzle, boundary conditions and the meshes.

The boundary layer is set on the inner wall of the two-dimensional axisymmetric nozzle, and the mesh is generated within the nozzle and downstream space. On the basis of the principle of $y+ < 1$ and in combination with the computational parameters, the minimum grid size applicable to all cases is estimated to be $\Delta l_{min} < 26$ μm. In practice, we set the boundary layer near the wall to 10 μm and then gradually transition to a global grid size of 0.8 mm.

Table 1 presents the detailed sizes of the two-dimensional axisymmetric nozzles. The positions l_{inj} and angles λ_{inj} of the annular injectors are adjustable. The operation pressure is set to 101325 Pa. Both inlets stagnation temperatures are remained at a constant 300 K (equal to the wall temperature and the atmosphere).

Table 2 presents the inlet pressure settings for the main nozzle and bypass injector, as well as the particle inlet conditions. Table 3 displays the grid sizes and numbers of grids for the five different grids obtained by controlling the mesh size in the nonboundary layer region during the grid independence validation calculation. Table 4 presents the case conditions used to investigate the effects of different parameters on the flow characteristics.

To compare the Loth, Henderson, and newly developed models' performance, all of which account for gas compressibility, rarefaction, and inertia effects. Initially, a rectangular de Laval nozzle 3D geometry is employed, as adopted by Meyer; the structure and specific dimensions are illustrated in Fig. 2 and detailed in Table 5.

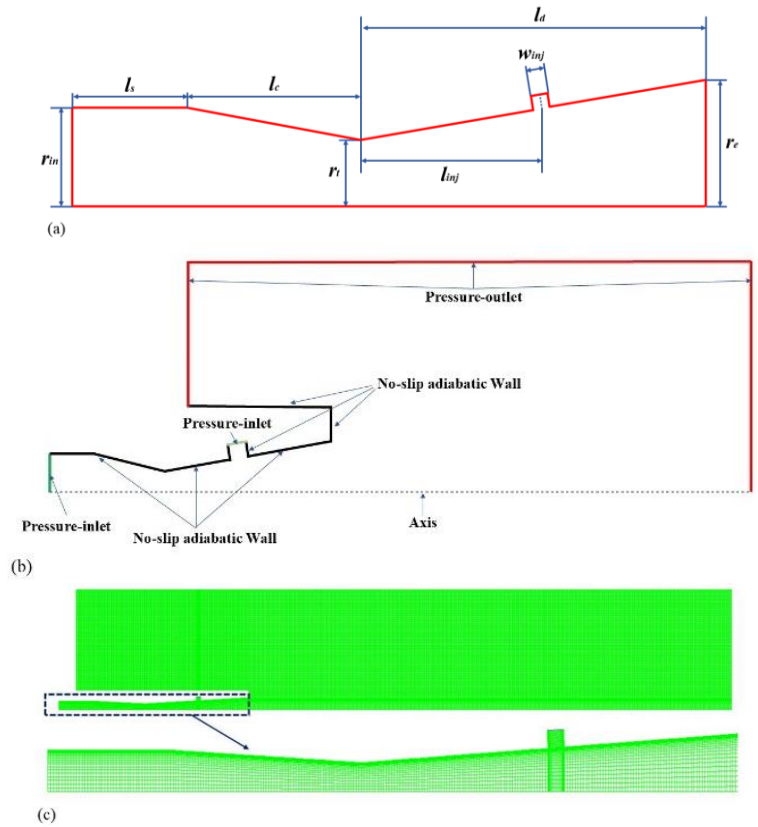

Fig. 1 (a) 2D axisymmetric nozzle outline sketch, (b) nozzle calculation domain and boundary conditions, and (c) nozzle global and local fine meshes

Table 3 Grid independence verification operation parameters

Case	Nonboundary layer area Mesh size	Grid number
	G_s, mm	
13	1.2	33183
13	1.1	75700
13	1.0	109638
13	0.8	128205
13	0.6	144508

Table 4 Calculation parameters and operational parameters of the injectors

Case	l_{inj}/(mm)	λ_{inj}/(°)	*NPR*	*SPR*
10	22.5	30	19.74	0.20
11	45.5	30	19.74	0.20
12	68.3	30	19.74	0.20
13	90.4	30	19.74	0.20
14	112.6	30	19.74	0.20
15	68.3	-45	19.74	0.20
16	68.3	-30	19.74	0.20
17	68.3	0	19.74	0.20
18	68.3	45	19.74	0.20
19	68.3	0	14.80	0.20
20	68.3	0	24.67	0.20
21	68.3	0	29.61	0.20
22	68.3	0	34.54	0.20
23	68.3	0	19.74	0.10
24	68.3	0	19.74	0.15
25	68.3	0	19.74	0.25
26	68.3	0	19.74	0.30

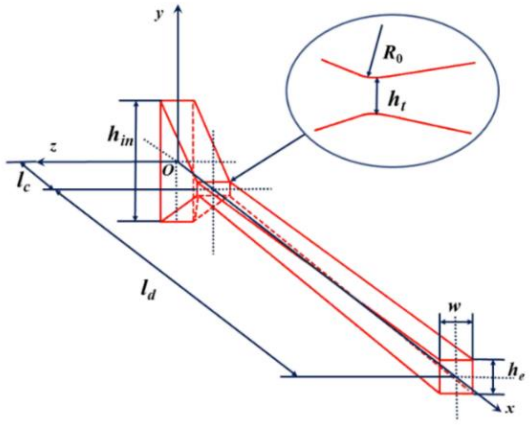

Fig. 2 3D nozzle structure sketch for verifying the drag coefficient model

Table 5 Detailed dimensional data of the three-dimensional nozzles

l_c, mm	l_d, mm	h_{in}, mm	h_t, mm	h_e, mm	R_0, mm	w, mm
30	120	17.72	1.02	3.8	10	3.07

During the validation of the drag models, we compare Loth, Henderson, and our own drag models, using two different materials, titanium and Stellite 21, for the calculations. The particle mass loadings used in the titanium calculations are 0.007, 0.025, 0.05, and 0.069, whereas those used in the Stellite 21 calculations were 0.07, 0.135, 0.212, 0.275, and 0.346. The nozzle inlet

stagnation pressure is p_{p0}=5.93 atm, the inlet static pressure is p_p=5.92 atm, and the particle diameter for injection is dp=30 μm, which is selected on the basis of the volume-averaged diameter measured in Meyer's experiments.

3.2 Jet-Flow Index Definition

To analyse gas–particle two-phase jet flow quantitatively, we define performance indicators.

$$v_{p,a} = \sum_{N_{cs}} N_p v_{p,x} / \sum_{N_{cs}} N_p \tag{22}$$

$$\Phi_{vp} = \sqrt{\sum_{N_{cs}} \left(N_p v_{p,x} - N_p v_{p,a}\right)^2} \Big/ \left(v_{p,a}^{NW} \sum_{N_{cs}} N_p\right) \tag{23}$$

$$\Psi_p = \sqrt{\sum_{N_{cs}} \left(N_p \zeta_p\right)^2} \Big/ \left(r_e \sum_{N_{cs}} N_p\right) \tag{24}$$

$v_{p,a}$ represents the acceleration effect of the particles, reflecting the acceleration effect and thereby determining the effective range of the fire extinguisher. Φ_{vp} denotes inhomogeneity of the particle velocity on flow direction, which is closely tied to the ultimate flow direction distribution range of the particles. Ψ_p denotes dispersion of the particles. The combinations of different magnitudes of $v_{p,a}$, Φ_{vp}, and Ψ_p can be tailored for different types of fires. Typically, a combination of high $v_{p,a}$ and low Ψ_p has a greater capability of penetrating target, thus penetrating fires is easier to extinguish under this combination. To extinguish the spreading fires, such as the combustion of liquid fuels, a moderate combination of $v_{p,a}$ and high Ψ_p is more effective. Also, for dispersed fires, a combination of high Ψ_p and Φ_{vp} is more effective. Here, ζ_p and v_{px} represent the radial coordinates and axial velocity components of the computational examples, respectively, whereas N_{cs} represents the number of particles in the cross-sectional unit grid.

3.3 Grid Independence Validation

To capture the nozzle throat, boundary layer of wall, and jet region in the two-dimensional axisymmetric nozzle, grid refinement is employed. Based on the y+<1 criterion, size of minimum grid can be estimated for all research scenarios: $\Delta lmin \leq 2.6$ μm. The first layer minimum grids size normal to the wall is set to 1 μm, other detail about the grid setting is shown in Table 3. Also, our test calculations show that the combination of the Courant–Friedrichs–Lewy number CFL=1 and time step equal to 10^{-6} s strikes a balance between solution accuracy and computational efficiency.

Figure 3 illustrates the variation in the average velocity at the nozzle outlet under the same boundary conditions for five different grid partitions. As the number of grids increases, the average velocity at the outlet decreases, which is due to the improvement in the computational accuracy. However, when the number of grids reaches a certain level, further increasing the number of grids does not significantly improve the computational accuracy, as evident from the similar results obtained for Grids 3, 4, and 5, with a relative difference of only 0.84% between Grids 3 and 4 and 0.32% between Grids 4 and 5. Moreover, an excessive number of grids can reduce the computational speed. Therefore, considering both computational accuracy and efficiency, we adopt Grid 4 as the optimal grid partition for subsequent research.

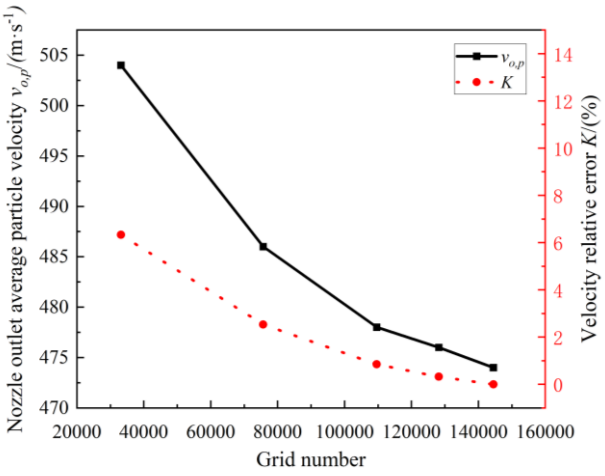

Fig. 3 Relationship between the number of grids and the average particle velocity at the nozzle outlet

3.4 Numerical Method and Drag Model Validation

All three drag models are outside the error bar range (Fig. 4). This is because this study considered only the case of monodisperse particle size distributions. Additionally, the use of experimentally measured volume-averaged diameter values may not accurately reflect the true average diameter. The range of the experimental data's error bar is ±5% of the measured values. By comparing with data of experiment, the simulation results for Ti particles exceed the error range by ±5.8% for our model, ±6.3% for the Loth model, and ±7.0% for the Henderson model (Fig. 4-a). For St particles, the results exceed ±9.9% for our model, ±12.2% for the Loth model, and ±30.8% for the Henderson model (Fig. 4-b).

The present model and the Loth model both demonstrate accuracy. The Henderson model performs better in simulating titanium particles but is less accurate in simulating Stellite 21 particles. Overall, the new model applied in our study has the best accuracy. The reason for this outcome is that the Loth (2021) model excessively corrects for rarefaction effects, whereas the Henderson (1976) model slightly under corrects for rarefaction effects. Notably, the predicted average particle velocity at the nozzle outlet for all the models is systematically greater than the measured value. In Meyer's study, there is likely a slight underestimation of the average diameter of the particle system involved, whereas in the actual experiment, there a certain size distribution.

Therefore, the model in this study overcomes the limitations of the Clift, Parmer, and Henderson models in terms of M_p and Re_p and accurately corrects the gas compressibility effect, rarefaction effect, and inertia effect over a wide range of M_p and Re_p. The excellent agreement between experiment data and calculated data proves effectiveness of numerical methods and the modelling framework in this study.

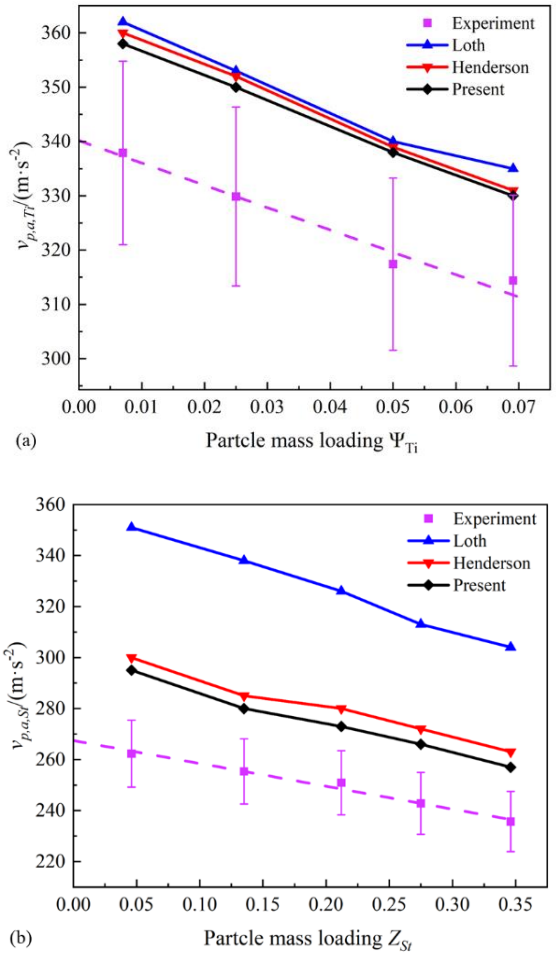

Fig. 4 Comparison of the three resistance models and the actual data for calculating the average velocity and particle mass load of titanium particles at the nozzle exit: (a) titanium and (b) Stellite 21

4. RESULTS AND ANALYSIS

This chapter analyses the effects of the geometric parameters (injection position l_{inj}, angle λ_{inj}) and injection conditions (main jet total pressure ratio NPR, injector total pressure ratio SPR) of the particles in a bypass injector on the flow field, and the effect on $v_{p,a}$, Φ_{vp}, and Ψ_p of the particles. Moreover, we conduct a centre of mass calculation for the dispersed particles and qualitatively analyse the impact of the centre of mass position on the movement (average axial acceleration $a_{p,ax}$, average radial acceleration $a_{p,ay}$) of the dispersed particles.

The coordinate system's origin in this study is set at the nozzle exit. We build a 2-D coordinate system via $X = (x - l_s - l_d - l_c)/d_e$ and $Y = y/d_e$. Generally, fire suppression systems in practical applications place a fire extinguishing target within the range of the jet core. For comprehensiveness and differential comparison, this study selects all jet performance indicators on two cross-sections corresponding to the jet startup section and the core section, with X=10 and 20, respectively, for parameter analysis. In the subsequent description, each indicator at X=10 and 20 (i.e., l_j=10d_e and 20d_e) is represented as ζ10 and ζ20 (ζ=$v_{p,a}$, Φ_{vp}, or Ψ_p), and the relationship between the particle acceleration at the nozzle exit (i.e., X=0) and each parameter is analysed.

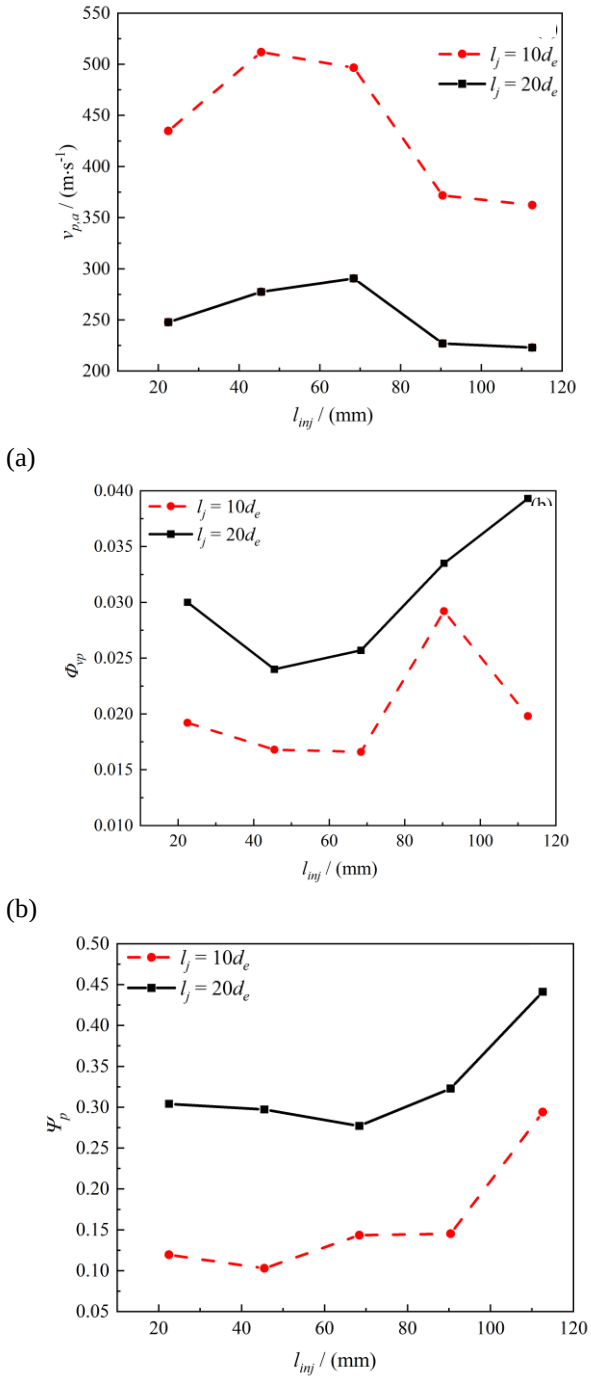

Fig. 5 Effects of bypass injector position l_{inj} on the (a) the average particle velocity $v_{p,a}$, (b) velocity inhomogeneity Φ_{vp}, and (c) particle dispersion Ψ_p

4.1 Effect of the Injection Position

The geometric parameters and operating parameters of the nozzle jointly affect the fire extinguishing efficiency. In this section, the influence of the geometric parameters on the nozzle position is first discussed. As the jet develops, $v_{p,a}$ decreases, and Φ_{vp} and Ψ_p increase (Fig. 5). This is because of the development of the boundary layer on the inner wall of the nozzle, leading to

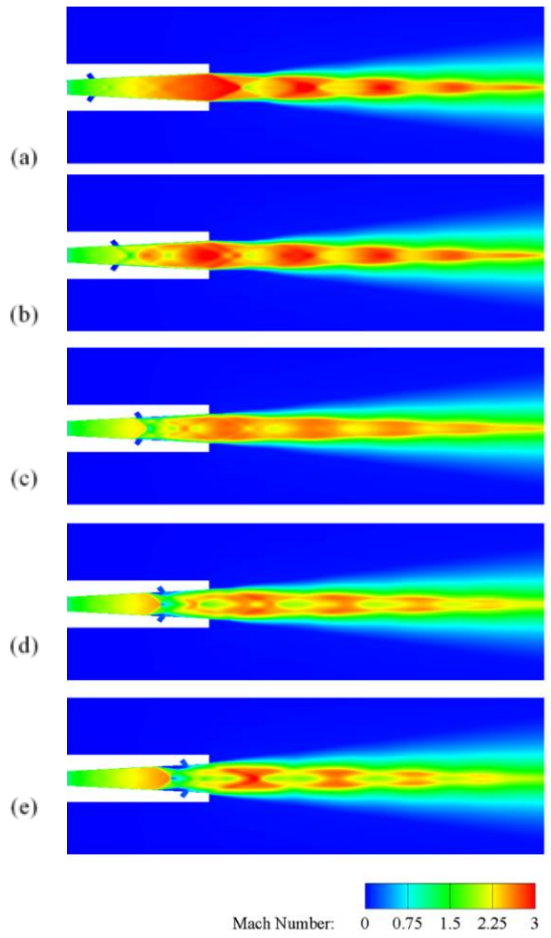

Fig. 6 Effects of bypass injector position l_{inj} on gas-phase Mach number contours: (a) l_{inj}=22.5 mm, (b) l_{inj}=45.5 mm, (c) l_{inj}=68.3 mm, (d) l_{inj}=90.4 mm, and (e) l_{inj}=112.6 mm

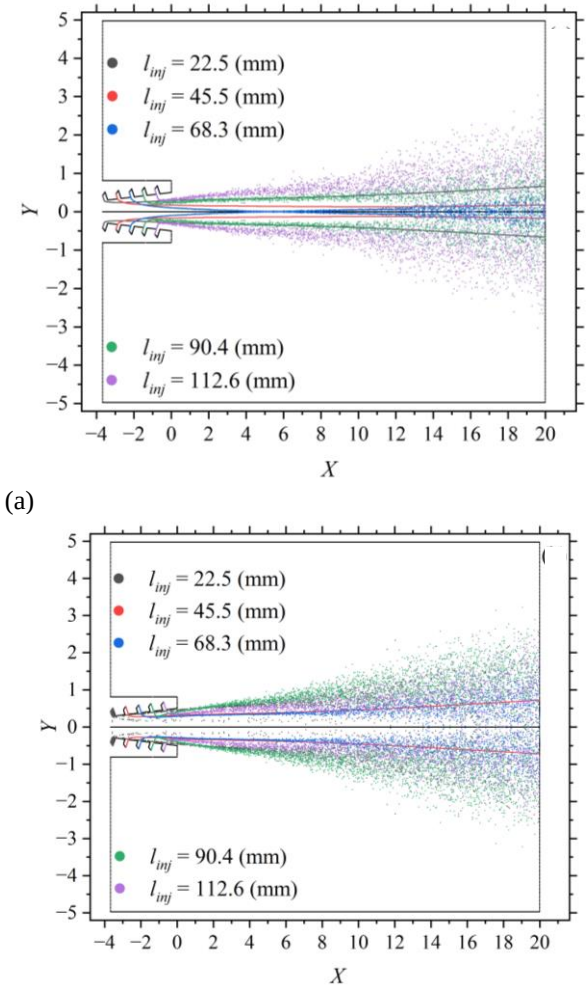

Fig. 7 Effect of bypass injector position l_{inj} on the particle trajectory: (a) particle ID=0 and (b) particle ID=33

the appearance of the downstream subsonic region, which increases the influence on the particle motion, inhibits the increase in the particle flow velocity, reduces its velocity, and disturbs the axial motion of the particles, leading to an increase in velocity inhomogeneity and particle dispersion. With increasing l_{inj}, $v_{p,a}$ first increases, $v_{p,a10}$ changes monotonicity at l_{inj}=45.5 mm, and $v_{p,a20}$ changes monotonicity at l_{inj}=68.3 mm. $v_{p,a10}$ and $v_{p,a20}$ reached peak values of 511.88 m/s and 290.54 m/s, respectively. $v_{p,a10}$ first increases by 15% and then decreases by 29%, and $v_{p,a20}$ first increases by 15% and then decreases by 23%. Φ_{vp} first decreases, Φ_{vp10} changes monotonicity at l_{inj}=68.3 mm and at l_{inj}=90.4 mm. Φ_{vp} and Φ_{vp10} reach minimum values of 0.0166 and 0.0240, respectively. Φ_{vp20} first decreases by 25% and then increases by 64%. Ψ_p first decreases, Φ_{vp10} changes monotonicity at l_{inj}=45.5 mm and Φ_{vp20} changes monotonicity at l_{inj}=68.3 mm, both reaching minimum values. Ψ_{p10} decreases by 16% and then increases by 185%. Ψ_{p20} decreases by 10% and then increases by 59%. When the nozzle position moves towards the nozzle outlet, there is a dramatic shift in the Mach reflection structure, size of incident oblique shock wave and central Mach disk increases, Mach disk position gradually approaches the nozzle outlet. However, as the Mach disk moves upstream relative to the injected flow, the Mach disk shock wave intensity also gradually increases, leading to an increase in the spatial range of the subsonic region in the wake of Mach disk and a drop in the Mach number. In addition, the gas expansion in the nozzle expansion section is limited.

Furthermore, as a result of the generation of more complex shock wave structures, the inhomogeneity of the gas velocity in core region of jet increases both axially and radially. Moreover, the positions of shock wave also change dramatically (Fig. 6).

Figure 7 shows the trajectories of average diameter particles injected at different nozzle positions l_{inj} from the most stream to the most downstream position of the nozzle entrance. The closer the nozzle position is to the throat of the nozzle, the greater the determinacy of the particle trajectories. Only at l_{inj}=68.3 mm do the particles achieve movement towards the centreline and pass through the centreline. At l_{inj}=22.5 mm, 90.4 mm, and 112.6 mm, the particles tend to move towards the wall, leaving the core region of the jet and reaching the external low-speed region. At l_{inj}=45.5 mm, the particle trajectory is always close to the centreline. In Fig. 7, the particles at l_{inj}=90.4 mm move radially outwards in the jet; therefore, the particle trajectory is closer to the wall.

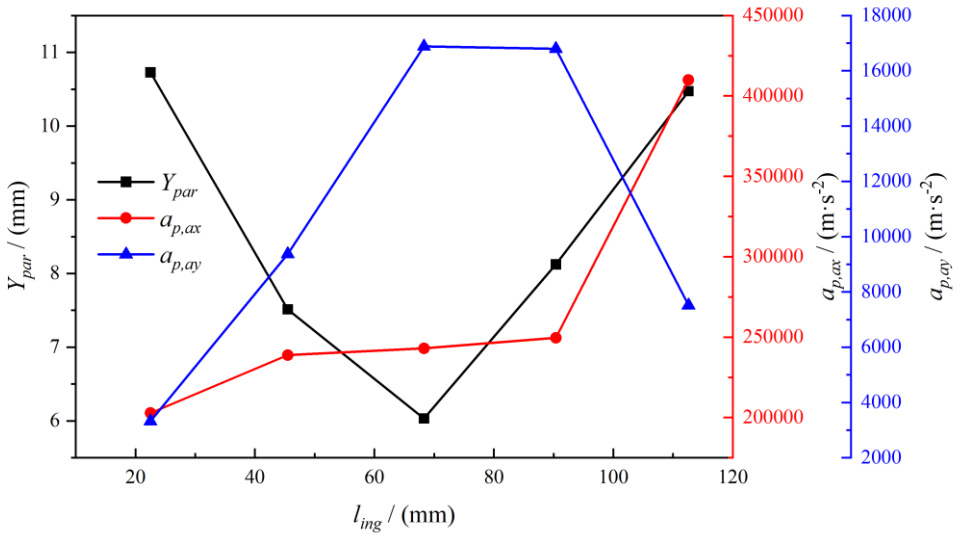

Fig. 8 Effects of bypass injector position l_{inj} on the particle acceleration component and virtual particle centroid

Figure 8 shows the variation in the average axial and radial accelerations of the particles with respect to the nozzle injection position. Within the nozzle exit section, as l_{inj} increases, the average axial acceleration $a_{p,ax}$ of the particles monotonically increases, indicating an increase in the relative velocity between the particles and the gas as the nozzle exit moves backwards. The reason for this change may be that the backwards movement of the nozzle reduces the acceleration time of the particles in the jet space, leading to a decrease in the particle velocity and an increase in the relative velocity. On the other hand, the average radial acceleration $a_{p,ay}$ does not change monotonically, changing monotonicity at l_{inj}=68.3 mm, increasing monotonically before this point, and decreasing after it (Fig. 8). According to the particle system momentum equation, particles in the nozzle exit section is considered as a virtual particle that experience a drag force along flow direction and resistance in lateral direction. The change in radial acceleration reflects the behaviour of the centre of mass of this virtual particle moving towards the centreline and crossing to the other side. The centre of mass of this virtual particle gradually approaches the centreline as l_{inj} increases, reaching its closest distance to the centreline at l_{inj}=68.3 mm (Fig. 8). In combination with the gas-phase flow field within the nozzle, when l_{inj}=22.5, the mass centre of the virtual particle is located in the high-speed gas region, where the gas lateral velocity gradient is small, resulting in a smaller radial acceleration component. When l_{inj}=45.5, the centre of mass of the virtual particle is located at the oblique shock wave, where the radial velocity gradient is large, leading to an increase in the radial acceleration. Similarly, as the centre of mass of the virtual particle first approaches and then moves away from the centreline, the velocity gradient at its location first increases, reaching a peak at l_{inj}=112.6, and then returns to a low-speed gas region, resulting in a decrease in the radial acceleration, as shown in the graph.

On the basis of the above analysis, we can summarize the selection of the nozzle injection position l_{inj} across various combustion modes. When l_{inj}=68.3 mm, $v_{p,a}$ reaches its peak of 290.54 m/s, and Ψ_p is minimal, at only 0.2771. Therefore, this nozzle is suitable for penetrating flames and has a greater ability to penetrate the target combustion material. When $v_{p,a}$ approaches 253.11 m/s and Ψ_p exceeds 0.3, the nozzle structure at l_{inj}=22.5 mm is more suitable for spreading flames. When l_{inj}=112.6 mm, the particle velocity inhomogeneity Φ_{vp} reaches the maximum value of 0.0393, and Ψ_p also reaches the maximum value of 0.4411. Therefore, this nozzle structure is suitable for dispersing flames.

4.2 Effect of the Injection Angle

In addition to the nozzle position, the nozzle angle is another geometric parameter that significantly impacts the firefighting capabilities. As the jet develops in the axial direction, the changes in $v_{p,a}$, Φ_{vp}, and Ψ_p are consistent with the analysis in the previous section. However, with increasing nozzle angle λ_{inj}, $v_{p,a}$ first increases but then decreases. Specifically, $v_{p,a10}$ reaches its maximum value of 543.35 m/s at λ_{inj}=0° and then monotonically decreases, whereas $v_{p,a20}$ reaches its maximum value of 323.01 m/s at λ_{inj}=-30°. Overall, Φ_{vp} shows an increasing trend, with Φ_{vp10} initially decreasing to a minimum of 0.0022 at λ_{inj}=-30° and then increasing, whereas Φ_{vp20} monotonically increases from a minimum value of 0.1830 to a maximum value of 0.2647. Ψ_p initially increases and then decreases, with Ψ_{p10} and Ψ_{p20} reaching their respective maximum values of 0.1435 and 0.2771 at λ_{inj}=30° (Fig. 9). Moreover, the influence of λ_{inj} on the Mach structure of the nozzle gas jet is not significant, as the upstream Ma profiles of the Mach reflection structure at various nozzle angles are very similar. In contrast, a significant intensification of the shock waves is observed as the nozzle angle transitions from λ_{inj}=30° to 45°. Additionally, the structure of the jet core region becomes more complex, and the Φ_{vp} in the flow and lateral directions increases (Fig. 10).

As the nozzle angle λ_{inj} increases, some particle trajectories with the same ID=0 have crossed the centreline. Specifically, at λ_{inj}=0°, the particles first cross the centreline, followed by λ_{inj}=-30°, 30°, and -45°. However, when λ_{inj}=45°, the particle trajectories do not cross the centreline (Fig. 11). For particles with the same

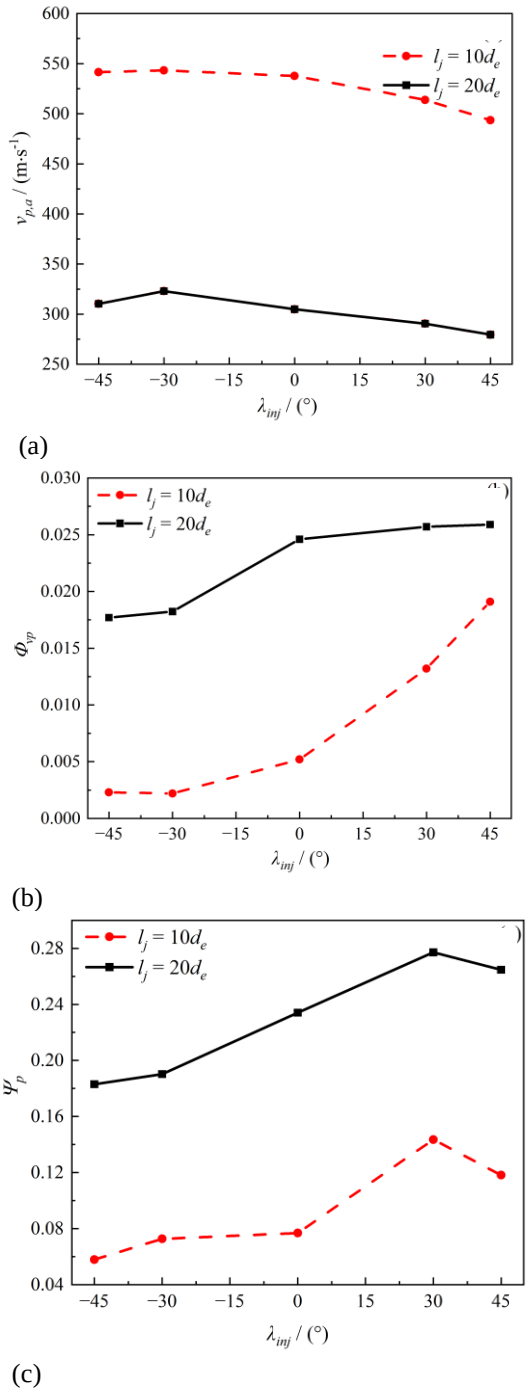

Fig. 9 Effects of bypass injector angle λ_{inj} on the (a) average particle velocity $v_{p,a}$, (b) velocity inhomogeneity Φ_{vp}, and (c) particle dispersion Ψ_p

ID=33, all trajectories do not pass through the centreline. The trajectories corresponding to the smallest injection angle always occupy positions closer to the centreline, and as λ_{inj} increases, the particle trajectories move further away from the centreline, occupying more external positions in the subsequent stages.

With increasing nozzle angle λ_{inj}, the axial acceleration, $a_{p,ax}$, increases, changing monotonicity at λ_{inj}=-30° and again at λ_{inj}=30° (Fig. 12). The change in λ_{inj} affects the initial velocity components of the particles in the axial and radial directions within the nozzle. In the axial direction, the initial velocity of the particles

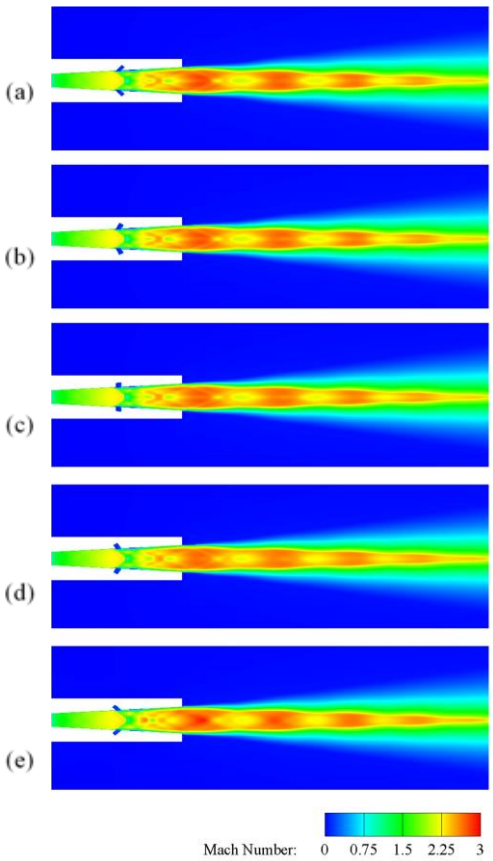

Fig. 10 Effect of bypass injector position λ_{inj} on gas-phase Mach number contours: (a) λ_{inj}=-45°, (b) λ_{inj}=-30°, (c) λ_{inj}=0°, (d) λ_{inj}=30°, and (e) λ_{inj}=45°

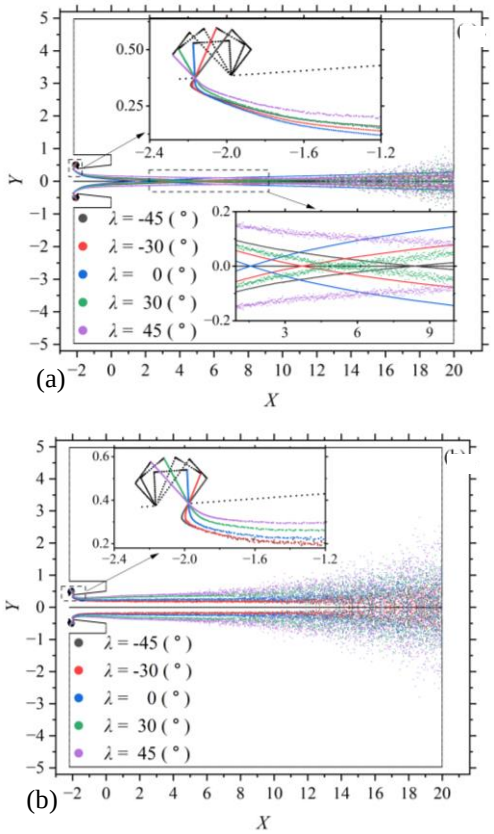

Fig. 11 Effects of the bypass injector angle λ_{inj} on the particle trajectory: (a) particle ID=0 and (b) particle ID=33

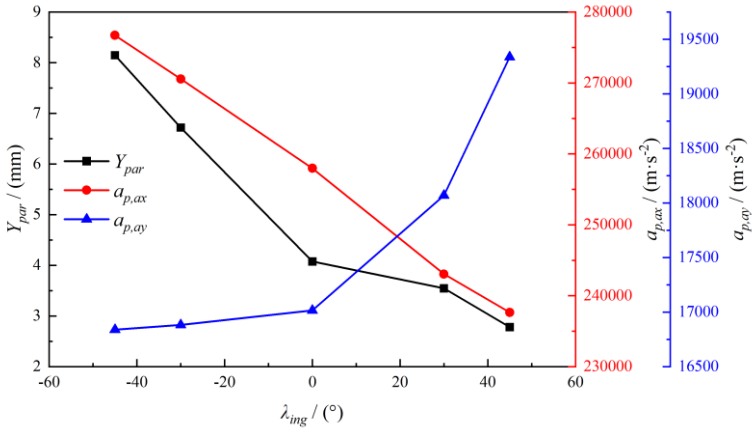

Fig. 12 Effects of the bypass injector angle λ_{inj} on the particle acceleration component and virtual particle centroid

monotonically increases from a negative initial velocity, reaching the maximum speed at λ_{inj}=45°. Analysis of the gas phase Mach contour diagram reveals that a change in λ_{inj} has a smaller influence on the flow pattern within the nozzle. Therefore, the alteration of initial particle velocity has a greater influence on $a_{p,ax}$ than does the change to gas flow field. As the axial velocity component of the virtual particle continuously increases, the relative axial velocity between the particles and the flow field decreases, gradually reducing $a_{p,ax}$. The relationship between $a_{p,ax}$ and the angle can also account for the gradual decline in $v_{p,a10}$ and $v_{p,a20}$ as the angle increases.

For the radial direction, similar to the analysis in the previous section, the particles within this section are considered virtual particles, and the acceleration components of these virtual particles are analysed. The change in the centre of mass of the virtual particle is shown in Fig. 12. As the nozzle angle increases, the position of the centre of mass gradually moves closer to the centreline. Combining this with the gas phase Mach contour diagram, it is evident that the centre of mass gradually moves from the high-speed gas region towards the oblique shock wave in the centre of the flow field. In this process, the velocity gradient of the gas gradually increases, leading to a gradual increase in the radial acceleration component, $a_{p,ay}$, of the virtual particle.

On the basis of the above analysis, we can summarize the selection of the nozzle angle λ_{inj} under various flame conditions. When λ_{inj}=-30°, $v_{p,a}$ attains its peak value of 323.01 m/s, and Ψ_p converges to a minimum of 0.1902. This nozzle configuration exhibits enhanced penetration capability into the target combustion material, rendering it more suitable for suppressing penetrating flame. When $v_{p,a}$ approaches 300 m/s, Ψ_p exceeds 0.2, the nozzle structure at λ_{inj}=0° proves more suitable in suppressing flame spread. When the particle velocity inhomogeneity Φ_{vp} approaches its maximum value of 0.0259 and Ψ_p also approaches its maximum value of 0.2771, the selection of λ_{inj}=30° and 45° is suitable for dispersing flames.

4.3 Effect of Injecting NPR

In addition to the geometric structure of the nozzle, the operational parameters of the nozzle are crucial factors influencing the efficiency of particle fire extinguishing. This section analyses the influence of the main nozzle pressure ratio (*NPR*). In practice, a larger *NPR* means that the inlet pressure of the main nozzle is greater, providing the particles with greater kinetic energy. As the main *NPR* increases, both $v_{p,a}$ and Φ_{vp} monotonically increase, whereas Ψ_p initially increases. At *NPR*=24.67, Ψ_{p10} and Ψ_{p20} reach their respective maximum values of 0.1065 and 0.2816, respectively, and then decrease. The monotonicity changes at *NPR*=29.61 and then continues to increase. Specifically, $v_{p,a10}$ increases from 520.90 m/s to 559.05 m/s, an increase of 7.32%, whereas $v_{p,a20}$ increases from 286.72 m/s to 395.65 m/s, an increase of 36.71%. Ψ_{p10} increases from 0.0027 to 0.0110, a 307.40% increase, and Ψ_{p20} increases from 0.0204 to 0.0278, a 36.27% increase (Fig. 13). On the other hand, the increase in the *NPR* significantly affects the Mach structure of the jet flow. As the *NPR* increases, the Ma profiles of the Mach reflection structure inside the nozzle are very similar. However, in the jet flow region outside the nozzle, a larger *NPR* leads to more pronounced fluctuations in the gas flow parameters, and there is a significant increase in shock waves (Fig. 14).

An examination of the trajectories of particles reveals that as the *NPR* increases, the trajectories of the particles have more difficulty crossing the centreline. For instance, at *NPR*=14.80, the trajectories of particles with ID=0 intersect the X-axis at a point closer to *X*=0, and as the *NPR* increases, this intersection point gradually moves backwards. At *NPR*=34.54, the intersection point is farthest from *X*=0 (Fig. 15-a). Additionally, the particles trajectories introduced at the nozzle's most downstream location, specifically those with ID=33, do not cross the centreline, and ultimately, the particle trajectories merge together (Fig. 15-b).

On the basis of the acceleration components, we can examine the impact of the *NPR*. As the *NPR* increases, both the axial and radial particle accelerations monotonically increase. This indicates that with increasing *NPR*, the gas velocity at the nozzle exit in the axial and radial directions also increases, leading to a monotonic increase in the relative velocities along these directions. At the nozzle exit, considering all the particles

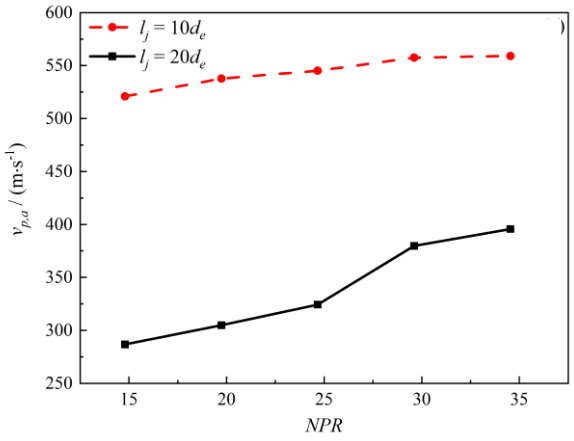

(a)

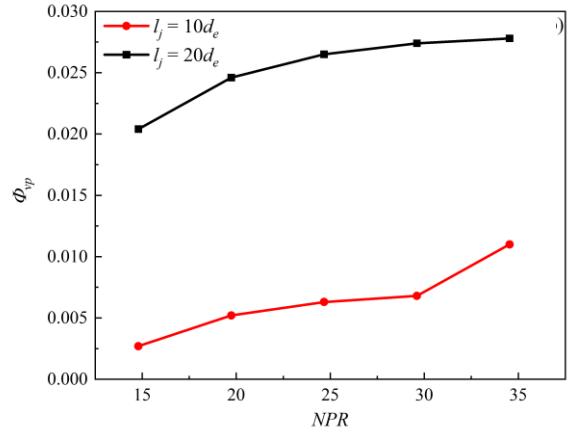

(b)

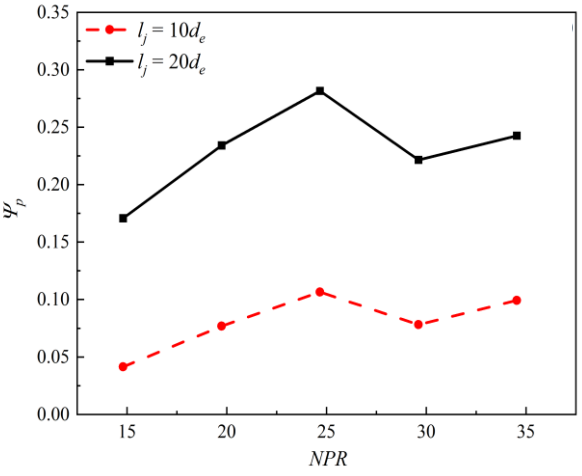

(c)

Fig. 13 Effects of the nozzle pressure ratio *NPR* on (a) average particle velocity $v_{p,a}$, (b) velocity inhomogeneity Φ_{vp}, and (c) particle dispersion Ψ_p

within the interface as a virtual particle, both $a_{p,ax}$ and $a_{p,ay}$ increase with increasing *NPR* (Fig. 16). This indicates that with increasing *NPR*, the gas velocity within the nozzle continuously increases in the axial direction, leading to a monotonic increase in $a_{p,ax}$, which can also explain the

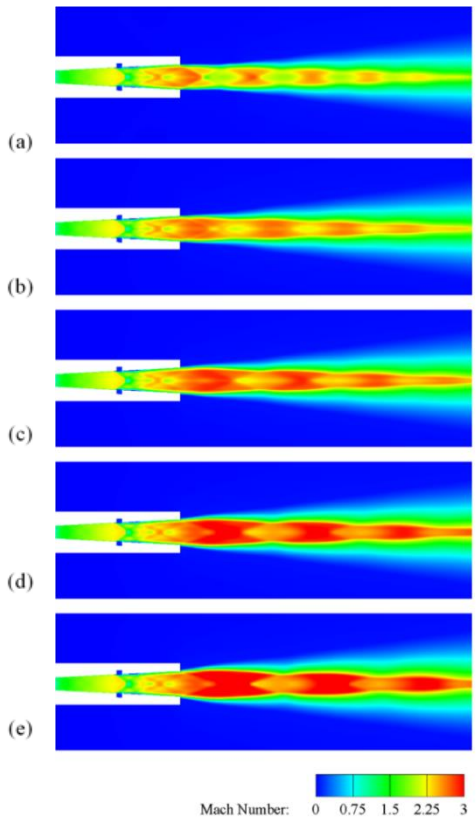

Fig. 14 Effect of the nozzle pressure ratio *NPR* on the gas-phase Mach number contours: (a) *NPR*=14.80, (b) *NPR*=19.74, (c) *NPR*=24.67, (d) *NPR*=29.61, and (e) *NPR*=34.54

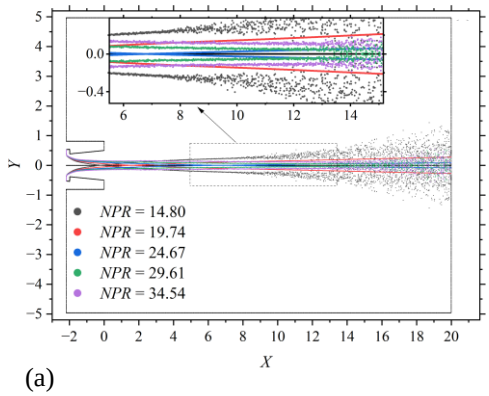

(a)

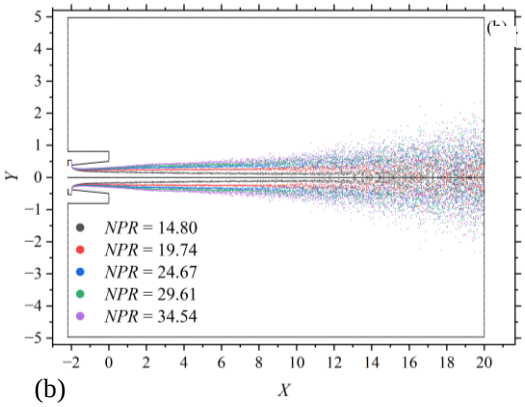

(b)

Fig. 15 Effect of the nozzle pressure ratio (*NPR*) on the particle trajectory: (a) particle ID=0 and (b) particle ID=33

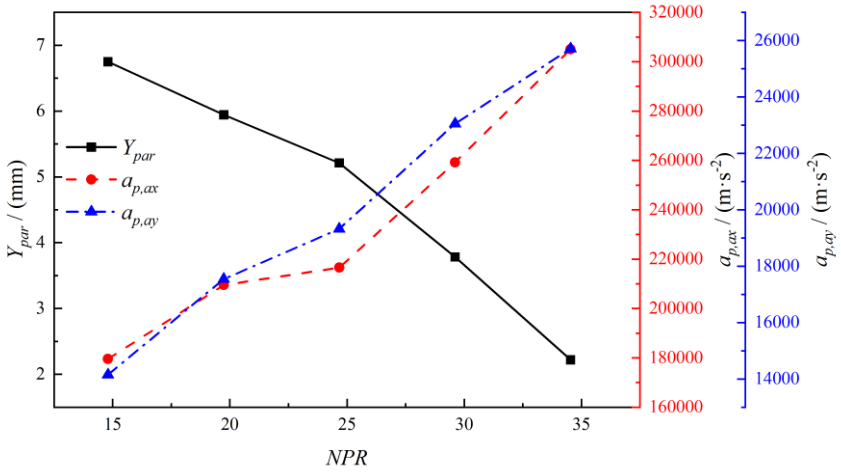

Fig. 16 Effect of the nozzle pressure ratio (*NPR*) on the particle acceleration component and virtual particle centroid

trend of $v_{p,a}$ (Fig. 16). Similarly, considering all selected particles as a virtual particle, the centre of mass of the virtual particle continuously moves closer to the centreline in the radial direction, shifting from the high-speed gas region with a smaller velocity gradient towards the low-speed gas region with a larger velocity gradient. Consequently, both factors lead to a monotonic increase in $a_{p,ay}$ (Fig. 16).

In summary, for different types of flames, the selection of the main nozzle pressure ratio (*NPR*) can be based on the following criteria: When the average particle velocity v_p exceeds 324.29 m/s and the dispersion Ψ_p is less than 0.2301, employing *NPR*=29.61 for the injection condition yields enhanced penetration capability into the target combustion material, thereby rendering it suitable for suppressing penetrating flame. When the axial velocity $v_{p,a}$ approaches 338.34 m/s and the dispersion coefficient Ψ_p exceeds 0.2301, *NPR*=24.67 is suitable for spreading flames. For *NPR*=34.54, when the particle velocity inhomogeneity Φ_{vp} reaches its maximum value of 0.0278 and when Ψ_p exceeds 0.2301, this injection condition is more suitable for dispersing flames.

4.4 Effect of Injecting SPR

In addition to the main nozzle pressure ratio (*NPR*), the injector total pressure ratio (*SPR*) is also an operational parameter that affects the firefighting capabilities. This section analyse the impact of the SPR. $v_{p,a}$ initially decreases and then increases, with $v_{p,a10}$ and $v_{p,a20}$ reaching their minimum values at 354.28 m/s and 205.22 m/s, respectively, before increasing. Compared with the maximum at *SPR*=0.10, $v_{p,a10}$ and $v_{p,a20}$ decrease by 36.11% and 37.90%, respectively. The behaviour of Φ_{vp} and Ψ_p is completely opposite to that of $v_{p,a}$. In the range of *SPR*=0.10.25, Φ_{vp} and Ψ_p monotonically increase, whereas in the range of *SPR*=0.250.3, Φ_{vp} and Ψ_p monotonically decrease. Φ_{vp10}, Φ_{vp20}, Ψ_{p10}, and Ψ_{p20} reach their maximum values at *SPR*=0.25, at 0.023, 0.0410, 0.2259, and 0.5353. Compared with the minimum values at *SPR*=0.10, Φ_{vp10}, Φ_{vp20}, Ψ_{p10}, and Ψ_{p20} increase by 2455.66%, 241.67%, 469.02%, and 275.91%, respectively. These results

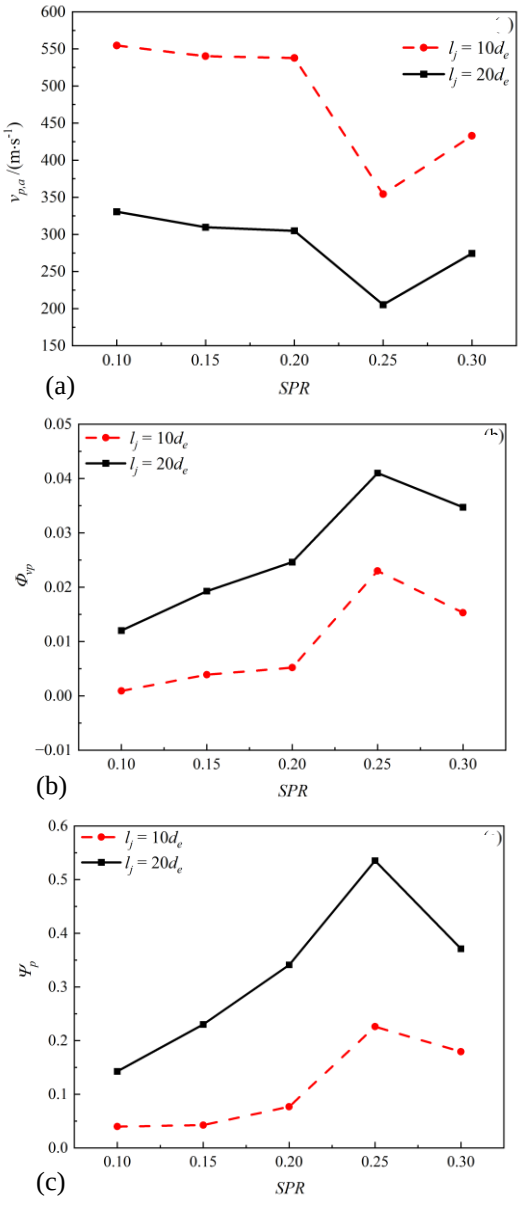

Fig. 17: Effects of the stagnation pressure ratio *SPR* on the (a) average particle velocity $v_{p,a}$, (b) velocity inhomogeneity Φ_{vp}, and (c) particle dispersion Ψ_p

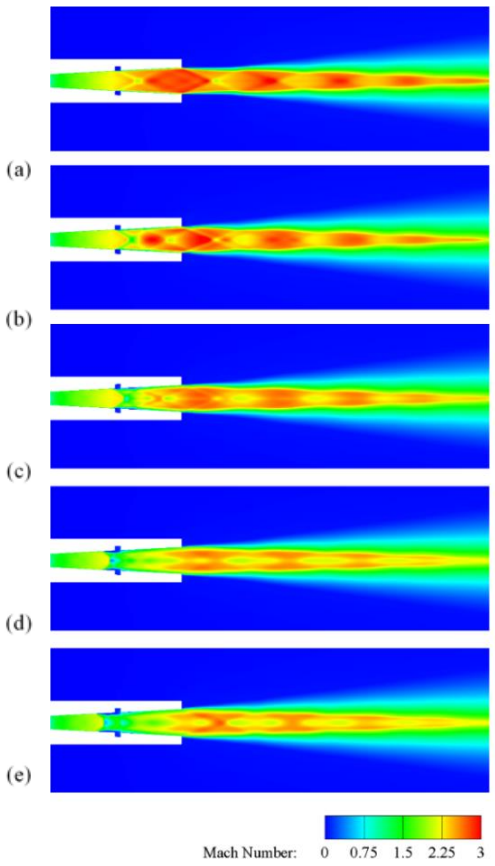

Fig. 18 Effect of the stagnation pressure ratio SPR on the gas-phase Mach number contours: (a) NPR=0.10, (b) NPR=0.15, (c) NPR=0.20, (d) NPR=0.25, and (e) NPR=0.30

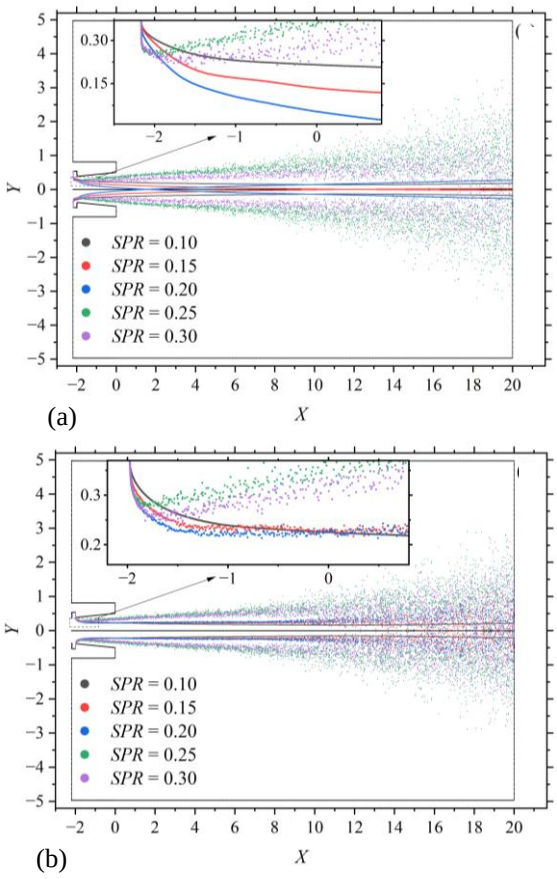

Fig. 19 Effect of the stagnation pressure ratio *SPR* on the particle trajectory: (a) particle ID=0 and (b) particle ID=33

indicate that the change in the *SPR* has a significant effect on the particle motion in the jet flow. Additionally, as the *SPR* increases, Mach reflection structure changes significantly. Consequently, the downstream subsonic region of the Mach disk expands, and the gas velocity inhomogeneity in the axial and radial directions in the jet core region increases. Furthermore, the positions of the shock waves also change significantly.

Trajectory analysis of particles introduced at the nozzle entrance extremities reveals that increasing *SPR* leads to a decline in trajectory certainty (Fig. 19). For particles with ID=0, at *SPR*=0.20, the trajectories first intersect the centreline, and then, at *SPR*=0.15, the trajectories intersect the centreline, with the intersection point located after the intersection point at *SPR*=0.20. The trajectories of the particles injected at *SPR*=0.25 and 0.30 tend to move towards the wall of the nozzle, away from the centreline. Similarly, the trajectories of particles with ID=33 do not cross the centreline, and for larger *SPRs*, the trajectories move further away from the centreline and closer to the wall.

Next, we analyse the impact of the SPR from the perspective of the acceleration components. As the *SPR* increases, $a_{p,ax}$ initially increases, reaching its maximum value of 28244.891 at *SPR*=0.15, then decreases, changing monotonicity at *SPR*=0.25 and then increases again, whereas $a_{p,ay}$ decreases with increasing *SPR* (Fig. 20). In the flow direction, the virtual particle's acceleration first decreases then increases. The change in $a_{p,ax}$ is caused by the increase in the *SPR*, which suppresses the Mach strength within the nozzle, resulting in a decrease in the gas velocity at the nozzle exit. Consequently, the relative velocity between the virtual particle and the gas at the nozzle exit decreases, resulting in a decrease in the axial acceleration. Combined with Fig. 18, it is evident that at *SPR*=0.25, the Mach strength within the nozzle is at its lowest, resulting in less acceleration than that at *SPR*=0.20 or 0.30. Similarly, in the radial acceleration component analysis, considering a virtual particle ensemble comprising exit-section particles, the centre of mass of the virtual particle gradually approaches the centreline as the *SPR* increases, moving away from the centreline to a distance of 11.2 mm at *SPR*=0.25, and then moving closer to the centreline (Fig. 20). This pattern of change aligns with the trajectories of the particles in Fig. 19, where the trajectories of the particles at *SPR*=0.10, 0.15, and 0.20 are closer to the centreline than those at *SPR*=0.25 and 0.30. Combined with the Mach contour diagram, it is evident that as the *SPR* increases, the mass centre of the virtual particle ensemble traverses the flow field, crossing from the high-velocity zone through the oblique shock wave into the low-speed gas region and then back into the high-speed gas region, ultimately settling in the region of the oblique shock wave. The analysis of the radial velocity gradients in different regions reveals that there is a correspondence between the changes in the velocity

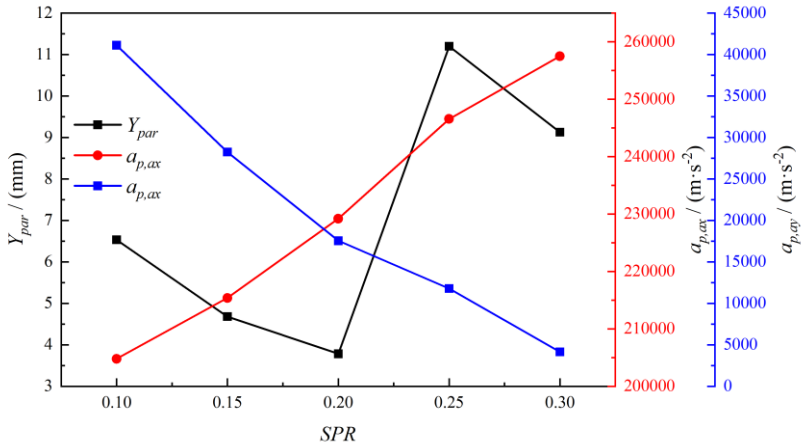

Fig. 20 Effects of the stagnation pressure ratio SPR on the particle acceleration component and virtual particle centroid

gradients and the trends in the radial acceleration component of the virtual particle. Overall, the impact of the *SPR* on the particle motion in the jet flow is significant, leading to changes in the acceleration components. The Mach strength within the nozzle, as well as the changes in the velocity gradients in different regions, plays a crucial role in the observed trends.

In conclusion, for various flame types, the selection of the *SPR* can be based on the following criteria.

For example, when $v_{p,a}$ reaches its peak of 330.49 m/s and minimal Ψ_p of 0.1424, injection condition of *SPR*=0.1 is ideal for controlling penetrating flames. Conversely, when particle velocities $v_{p,a}$ approach 284.9 m/s and dispersion Ψ_p exceeds 0.3239, an SPR of 0.3 proves more efficient for controlling spreading flames. For *SPR*=0.25, when the particle velocity inhomogeneity Φ_{vp} reaches its maximum value of 0.041 and Ψ_p also reaches its maximum value of 0.5353, this injection condition is more effective for dispersing flames.

5. CONCLUSION

This study investigates the impact of geometric parameters (injection position l_{inj}, angle λ_{inj}) and operational conditions (main nozzle pressure ratio *NPR*, injector total pressure ratio *SPR*) of the gas–particle flow field is analysed, as well as performance indicators such as Φ_{vp}, $v_{p,a}$, and Ψ_p. Appropriate geometric parameters and operational conditions for different types of flames were selected, including spreading, penetrating, and dispersing flames. The primary outcomes of this study are:

Compared with previous experimental results, the modelling framework and numerical methods used in this study achieve a greater level of accuracy, thus providing thorough validation of the simulation results. The adopted resistance model is more accurate than other resistance models, as it incorporates modifications for fluid compressibility and particle volume fraction. Compared with the other models, the modified resistance model demonstrates significantly better performance in predicting the particle curtain motion.

Increasing the position, angle, and total pressure ratio of the injector typically results in a decrease in $v_{p,a}$, as well as an increase in Φ_{vp} and Ψ_p. An increase in the total pressure ratio of the main jet leads to increases in $v_{p,a}$ and Φ_{vp}. However, under specific conditions, the monotonic dependency of these parameters may be disrupted. For example, the performance indicators at the position of the injector near the throat of the jet and at a larger total pressure ratio of the injector, as well as $v_{p,a}$ at smaller injection angles and Ψ_p at larger injection angles, may disrupt monotonicity.

For a penetrating flame, the selection criteria are as follows: a moderate injector position at l_{inj}≈68.3 mm, a high main jet total pressure ratio *NPR*≥29.61, an injector angle λ_{inj}≤-30°, and an injector total pressure ratio *SPR*≤0.1. For a spreading flame, the criteria are as follows: a smaller injector position at l_{inj}≈22.5 mm, an injector angle λ_{inj}≈0°, a main jet total pressure ratio *NPR*≈24.67, and a relatively high injector total pressure ratio *SPR*≈0.3. For a dispersing flame, the criteria are as follows: a larger injector position at l_{inj}≥112.6 mm, a wide injector angle λ_{inj}≥30°, a high main jet total pressure ratio *NPR*≥34.54, and a moderate injector total pressure ratio *SPR*≈0.25.

CONFLICT OF INTEREST

The author declares that there are no conflicts of interest to disclose during the process of conducting this study and writing this paper. All the authors confirm that they have no economic interests or other potential conflicts with the results or conclusions of this study.

AUTHOR CONTRIBUTION

Lite Zhang: Conceptualization, Methodology, Project administration, Resources, Supervision; **Sifan Wu:** Data curation, Investigation, Formal analysis, Writing–original draft, Visualization; **Yang Feng:** Investigation, Software, Validation; **Hao Guan:** Writing–review & editing.

REFERENCES

Bhattacharya, S., Lutfurakhmanov, A., Hoey, J. M., Swenson, O. F., Mahmud, Z., & Akhatov, I. S. (2013). Aerosol flow through a converging-diverging micro-nozzle. *Nonlinear Engineering*, *2*(3-4), 103-112. https://doi.org/10.1515/nleng-2013-0020

Cao, C., Han, T., Xu, Y., Li, W., Yang, X., & Hu, K. (2020). The associated effect of powder carrier gas and powder characteristics on the optimal design of the cold spray nozzle. *Surface Engineering*, *36*(10), 1081-1089. https://doi.org/10.1080/02670844.2020.1744297

Clift, R., Grace, J. R., & Weber, M. E. (1978). *Bubbles, drops, and particles.* Academic Press. https://doi.org/10.1080/07373939308916817

Foias, C., Manley, O., Rosa, R., Temam, R., & Mayer, M. E. (2002). Navier-stokes equations and turbulence. *Physics Today*, *55*(10), 54-56.

Gilbert, M., Davis, L., & Altman, D. (1955). Velocity lag of particles in linearly accelerated combustion gases. *Journal of Jet Propulsion*, *25*(1), 26-30. https://doi.org/10.2514/8.6578

Gosman, A., & Loannides, E. (1983). Aspects of computer simulation of liquid-fueled combustors. *Journal of Energy*, *7*(6), 482-490.

Haiqiang, L., Ruowen, Z., Jiaxin, G., Siuming, L., & Yuan, H. (2014). A good dry powder to suppress high building fires. *APCBEE Procedia*, *9*, 291-295. https://doi.org/10.1016/j.apcbee.2014.01.052

Henderson, C. B. (1976). Drag coefficients of spheres in continuum and rarefied flows. *AIAA Journal*, *14*(6), 707-708. https://doi.org/10.2514/3.61409

Jebakumar, A. S., & Abraham, J. (2016). Comparison of the structure of computed and measured particle-laden jets for a wide range of Stokes numbers. *International Journal of Heat and Mass Transfer*, *97*, 779-786. https://doi.org/10.1016/j.ijheatmasstransfer.2016.02.074

Ling, Y., Haselbacher, A., & Balachandar, S. (2011a). Importance of unsteady contributions to force and heating for particles in compressible flows. Part 2: Application to particle dispersal by blast waves. *International Journal of Multiphase Flow*, *37*(9), 1013-1025. https://doi.org/10.1016/j.ijmultiphaseflow.2011.07.002

Ling, Y., Haselbacher, A., & Balachandar, S. (2011b). Importance of unsteady contributions to force and heating for particles in compressible flows: Part 1: Modeling and analysis for shock–particle interaction. *International Journal of Multiphase Flow*, *37*(9), 1026-1044. https://doi.org/10.1016/j.ijmultiphaseflow.2011.07.001

Ling, Y., Wagner, J., Beresh, S., Kearney, S., & Balachandar, S. (2012). Interaction of a planar shock wave with a dense particle curtain: Modeling and experiments. *Physics of Fluids*, *24*(11). https://doi.org/10.1063/1.4768815

Parmar, M., Haselbacher, A., & Balachandar, S. (2010). Improved drag correlation for spheres and application to shock-tube experiments. *AIAA Journal*, *48*(6), 1273-1276. https://doi.org/10.2514/1.J050161

Parmar, M., Haselbacher, A., & Balachandar, S. (2011). Generalized Basset-Boussinesq-Oseen equation for unsteady forces on a sphere in a compressible flow. *Physical Review Letters*, *106*(8), 084501. https://doi.org/10.1103/PhysRevLett.106.084501

Ranz, W. E., & Marshall, W. R. (1952). Evaporation from drops – Part 1. *Chemical Engineering Progress*, *48*, 141-148.

Soliman, S., Abdallah, S., Gutmark, E., & Turner, M. G. (2011). Numerical simulation of microparticles penetration and gas dynamics in an axi-symmetric supersonic nozzle for genetic vaccination. *Powder Technology*, *208*(3), 676-683. https://doi.org/10.1016/j.powtec.2011.01.008

Sutherland, W. (2009). The Viscosity of gases and molecular force. *Philosophical Magazine*, *Edinburgh*, (36), 507-531. https://doi.org/10.1080/14786449308620508

Wang, Y., Shen, J., Yin, Z., & Bao, F. (2021). Numerical simulation of non-spherical submicron particle acceleration and focusing in a converging–diverging micronozzle. *Applied Sciences*, *12*(1), 343. https://doi.org/10.1080/02786820600615063

Zhang, W., Tainaka, K., Ahn, S., Watanabe, H., & Kitagawa, T. (2018). Experimental and numerical investigation of effects of particle shape and size distribution on particles' dispersion in a coaxial jet flow. *Advanced Powder Technology*, *29*(10), 2322-2330. https://doi.org/doi.org/10.1016/j.apt.2018.06.008

Zhu, Y., Cai, W., Wen, C., & Li, Y. (2009). Numerical investigation of geometry parameters for design of high performance ejectors. *Applied Thermal Engineering*, *29*(5-6), 898-905. https://doi.org/10.1016/j.applthermaleng.2008.04.025